VISCOACOUSTIC REVERSE-TIME MIGRATION

EMMANUEL CAUSSE[1,2] and BJØRN URSIN[2]

[1] *SINTEF Petroleum Research, N-7465 Trondheim, Norway.*
[2] *Department of Petroleum Engineering and Applied Geophysics, The Norwegian University of Science and Technology, S.P. Andersensv. 15A, N-7491 Trondheim, Norway.*

(Received April 22, 2000; revised version accepted July 20, 2000)

ABSTRACT

Causse, E. and Ursin, B., 2000. Viscoacoustic reverse-time migration. *Journal of Seismic Exploration*, 9: 165-184.

Absorption decreases the amplitude of waves propagating in the earth. In addition, it narrows the bandwidth and modifies the phase. Obtaining true-amplitude migration and acceptable resolution in dissipative media requires a migration algorithm that corrects these effects. To achieve this, a reverse-time prestack depth migration technique is used. This uses a stable *amplifying* finite-difference wavefield extrapolation that compensates for the *attenuating* propagation of the wavefields in the real earth. Numerical tests on synthetic VSP data illustrate how dissipation destroys the amplitude, phase and resolution in the migration images, and how our algorithm corrects these effects. The tests also show that the method is stable with respect to noise, and does not require a very detailed macro-model for dissipation.

KEY WORDS: migration, imaging, true-amplitude, high-resolution, attenuation, dissipation, absorption, finite-difference, representation theorem, adjoint medium.

INTRODUCTION

In the early days of seismic exploration, the unique goal of migration was to get structural information about the subsurface geology. Now, research focuses more on imaging the true reflectivity of the subsurface (e.g., Schleicher et al., 1993; Gray, 1997; Nicolétis et al., 1997). This requires a correct treatment of the factors affecting the amplitude of waves during the extrapolation and imaging steps of migration. One of these factors is intrinsic absorption. Most of today's migration algorithms consider the earth as a lossless acoustic

0963-0651/00/$5.00

or elastic medium and neglect the dissipation of waves. The presence of absorption (attenuation and dispersion) in real rocks affects the results of conventional and true-amplitude migration algorithms. Attenuation results in (1) a decrease in resolution; (2) an underestimation of the reflectivity, especially at large depths, and (3) velocity dispersion produces phase errors that complicate the detailed analysis of stratigraphy and the tying of migration images with well-log data (Stewart et al., 1984; De et al., 1994).

The first attempts to treat dissipation were directed towards the elimination of its effects from the data, by so-called inverse Q-filters (Robinson, 1979; Bickel and Natarajan, 1985). Since the effects of dissipation increase with the length of the wavepath, the filters are time-variant. Hargreaves and Calvert (1991) presented a technique for inverse-Q filtering of prestack data in 1-D media, that has a strong resemblance with Stolt migration.

Rather than compensating for the effects of absorption in a separate preprocessing step, however, it is more efficient to do it during the migration itself. This approach was followed by Dai and West (1994) for zero-offset migration, and by Mittet et al. (1995) for prestack migration. The idea is simple: since high frequencies are attenuated during the propagation in the earth from the source down to the reflectors and up to the receivers, the relative loss of high frequencies must be compensated for by boosting them during the extrapolation steps of migration. Causse and Ursin (1999) showed mathematically that, for a homogeneous medium, this gives a reflector image with (approximately) the correct phase, magnitude and resolution. The algorithms of Dai and West (1994) and Mittet et al. (1995) were based on downward continuation of the wavefields in the frequency-wavenumber domain. This presents some drawbacks: first, such methods may give inaccurate results in the presence of strong lateral velocity variations or steep dips. Second, they require a proper filtering of evanescent energy to avoid numerical unstability (Kosloff and Baysal, 1983). The stability of the extrapolation is a crucial point for a migration method that relies on the boosting of high frequencies.

We have developed a viscoacoustic reverse-time migration algorithm that does not present these drawbacks (the advantages of reverse-time migration are discussed by Levin (1984)). The wavefield extrapolation (with amplification) is performed by a high-order time-domain finite-difference method (Emmerich and Korn, 1987; Holberg, 1987; Mittet, 1994) where instability is avoided as explained by Appendix D of Causse et al. (1999), and the images are created by taking the zero-lag crosscorrelation between the downgoing and upgoing wavefields (Claerbout, 1971). This procedure is implemented for 2-D viscoacoustic migration, but the generalization to 3-D viscoelastic migration is straightforward. The method requires a macro-model for dissipation. This may be estimated, e.g., from VSP data as suggested by Amundsen and Mittet (1994), Harris et al. (1997) or Toverud and Ursin (1999).

To illustrate the method, we apply the algorithm to a 2-D synthetic Vertical Seismic Profile (VSP) data set. We show that viscoacoustic migration (correction for dissipation) gives better images than acoustic migration (no correction for dissipation), and that our algorithm has a low sensitivity to noncoherent noise and to the macro-model for dissipation.

VISCOACOUSTIC MIGRATION

In theory, the reflectivity at a point $\mathbf{x}$ in the subsurface can be obtained with the imaging formula of Claerbout (1971):

$$I(\mathbf{x}) = \int_{-\infty}^{\infty} d\omega [U(\mathbf{x},\omega)/D(\mathbf{x},\omega)] \quad , \tag{1}$$

where D and U represent the downgoing and upgoing pressure wavefields at $\mathbf{x}$, respectively. In a viscoacoustic medium, the reflection coefficient is slightly frequency-dependent so that the image $I(\mathbf{x})$ gives the reflectivity averaged over the frequency band of the incident wavefield. We calculate the downgoing wavefield D by finite-difference modelling in an attenuating viscoacoustic macro-model of the subsurface (Emmerich and Korn, 1987). To generate a pure downgoing incident field below the source, hard interfaces in the macro-model are smoothed by low-pass filtering. The upgoing reflected wavefield U is reconstructed by backward wavefield extrapolation. This involves a forward wavefield extrapolation in a fictive 'amplifying' macro-model (the adjoint of the attenuating viscoacoustic macro-model) with the time-reversed data as sources, as explained in Appendix A.

Equation (1) can be rewritten as

$$I(\mathbf{x}) = \int_{-\infty}^{\infty} W(\mathbf{x},\omega)\, U(\mathbf{x},\omega)\, D^{*}(\mathbf{x},\omega) d\omega \quad , \tag{2}$$

where the asterisk * denotes complex conjugation, and where $W(\mathbf{x},\omega)$ is a weighting operator which is necessary to obtain true-amplitude migration. The ideal imaging Equation (1) corresponds to a weighting

$$W(\mathbf{x},\omega) = 1/D(\mathbf{x},\omega)D^{*}(\mathbf{x},\omega) \quad . \tag{3}$$

In the case of a dissipation-free medium, the attenuating and amplifying viscoacoustic macro-models reduce to a single acoustic macro-model. In this case, Equation (3) gives

$$W_{ac}(\mathbf{x},\omega) \simeq \mathcal{L}^2(\mathbf{x})[1/|S(\omega)|^2] \quad , \tag{4}$$

where $\mathcal{L}^2(\mathbf{x})$ is the squared geometrical spreading from the source location to point $\mathbf{x}$, and $S(\omega)$ is the source spectrum. The operator (4), where the subscript $_{ac}$ refers to the acoustic (i.e., non-dissipative) case, contains a deconvolution and a correction for the effects of geometrical spreading in the migration image. Unfortunately the deconvolution is not stable because of zeroes in the source amplitude spectrum. In finite-difference implementations of reverse time migration, numerical dispersion at higher frequencies in the extrapolated wavefields represents high-frequency noise that makes the deconvolution particularly unstable. It is therefore usual to drop the deconvolution and define the weighting operator as

$$W_{ac}(\mathbf{x},\omega) = \mathcal{L}^2(\mathbf{x}) \quad . \tag{5}$$

In practice, $\mathcal{L}$ can be calculated by a geometrical approximation or by computing the energy in the downgoing wavefield during its numerical extrapolation.

In the case of a dissipative medium, the downgoing and upgoing wavefields D and U in Equation (2) both contain a frequency-dependent attenuation factor which should be removed by the weighting operator. The correction for the effects of dissipation would automatically be included if we could use the ideal weight function (3). However, in order to avoid the stability problems caused by the deconvolution, we propose to use the following weighting operator:

$$W_{va}(\mathbf{x},\omega) = \mathcal{L}^2(\mathbf{x})|D^A(\mathbf{x},\omega)|/[|D(\mathbf{x},\omega)| + \lambda] \quad , \tag{6}$$

where D^A is a downgoing field extrapolated in the amplifying macro-model, and λ is a small stabilization constant. The subscript $_{va}$ indicates that W_{va} is a viscoacoustic operator. If the medium is non-absorbing, this operator becomes equivalent to the acoustic operator (5). For a dissipative medium, operator (6) not only corrects the reflectivity values, but improves the resolution by compensating for the bandwidth reduction caused by attenuation. Equation (6), combined with viscoacoustic wavefield extrapolation and with the imaging equation (2), provides an image that is roughly speaking equal to the reflectivity convolved with a spatial version of the autocorrelation of the source wavelet (Causse and Ursin, 1999).

We see that numerical extrapolation with amplification is required in practice for both the reconstruction of the upgoing field (Appendix A) and for the weighting of the downgoing field.

NUMERICAL EXAMPLES

To test the method, we generated three common-receiver gathers by finite-difference modelling in a simple earth model with 2D walk-away VSP acquisition geometry (Fig. 1). The horizontal and vertical spacing between adjacent points of the finite-difference grid was 12.5 m. The effects of the free surface were not included in the modelling. To describe the viscoacoustic model, we used a standard linear solid parametrized by the density ρ, relaxation frequency ω_0, average between phase velocities at zero and infinite frequencies V_P, and minimum quality factor Q_{min} (see Appendix B). These parameters are given in Table 1. The phase velocity and the amplitude decay caused by attenuation are plotted in Fig. 2. We applied our algorithm to the vertical component of the particle velocity (Fig. 3). Because of the spatial reciprocity of wave propagation (Equation (A-6), the three walk-away VSP common-receiver records of the vertical component of the velocity are equivalent to three reversed-VSP common-shot pressure records (Mittet and Hokstad, 1995). Because the cost of the migration is directly related to the number of shots, processing the data as reversed VSP data is much more efficient. In the tests, the source function was the derivative of a Gaussian function. The pressure signal created by the dipole source in the vertical direction (i.e., the velocity receiver in the well, after applying the principle of reciprocity) is the derivative of this source function. This corresponds to a Ricker wavelet with main frequency 22 Hz. The source signature was assumed to be known. In practice, this signature could be obtained by source modelling (Landrø and Sollie, 1992; Amundsen, 1993; Landrø et al., 1994). The macro-model used for the migration was a low-pass filtered version of the exact model.

Table 1. Viscoacoustic model for the numerical test.

Layer	V_P (m/s)	Q_{min}	$\omega_0/2\pi$ (Hz)	ρ (kg/m^3)
I	1480	10000	18	1000
II	1870	42	14	1400
III	2180	31	20	2030
IV	2250	34	15	2090
V	2340	65	30	2160
VI	2380	30	20	2190
VII	2420	40	23	2210
VIII	2360	25	28	2180
IX	2520	30	18	2280
X	2650	26	20	2340
XI	2780	28	21	2380
XII	2690	32	24	2280
XIII	2820	40	26	2360

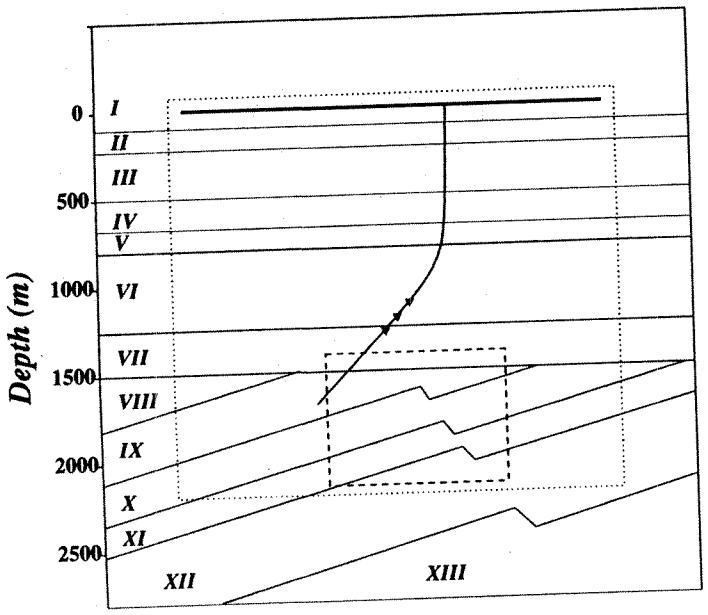

Fig. 1. Geometrical model and recording configuration for the numerical test. The dotted line delimits absorbing boundaries and the dashed line represents the target zone to be imaged. The shot locations are indicated by the bold line in layer I, and the receivers are marked by triangles above the target zone.

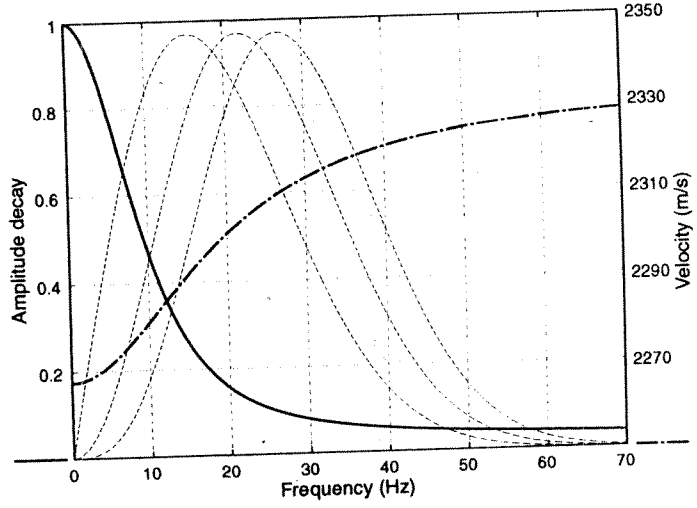

Fig. 2. Amplitude decay due to attenuation (solid line), and phase velocity (dashed-dotted line). The thin dashed lines represent the amplitude spectra of the source function, its first derivative (the Ricker wavelet), and its second derivative.

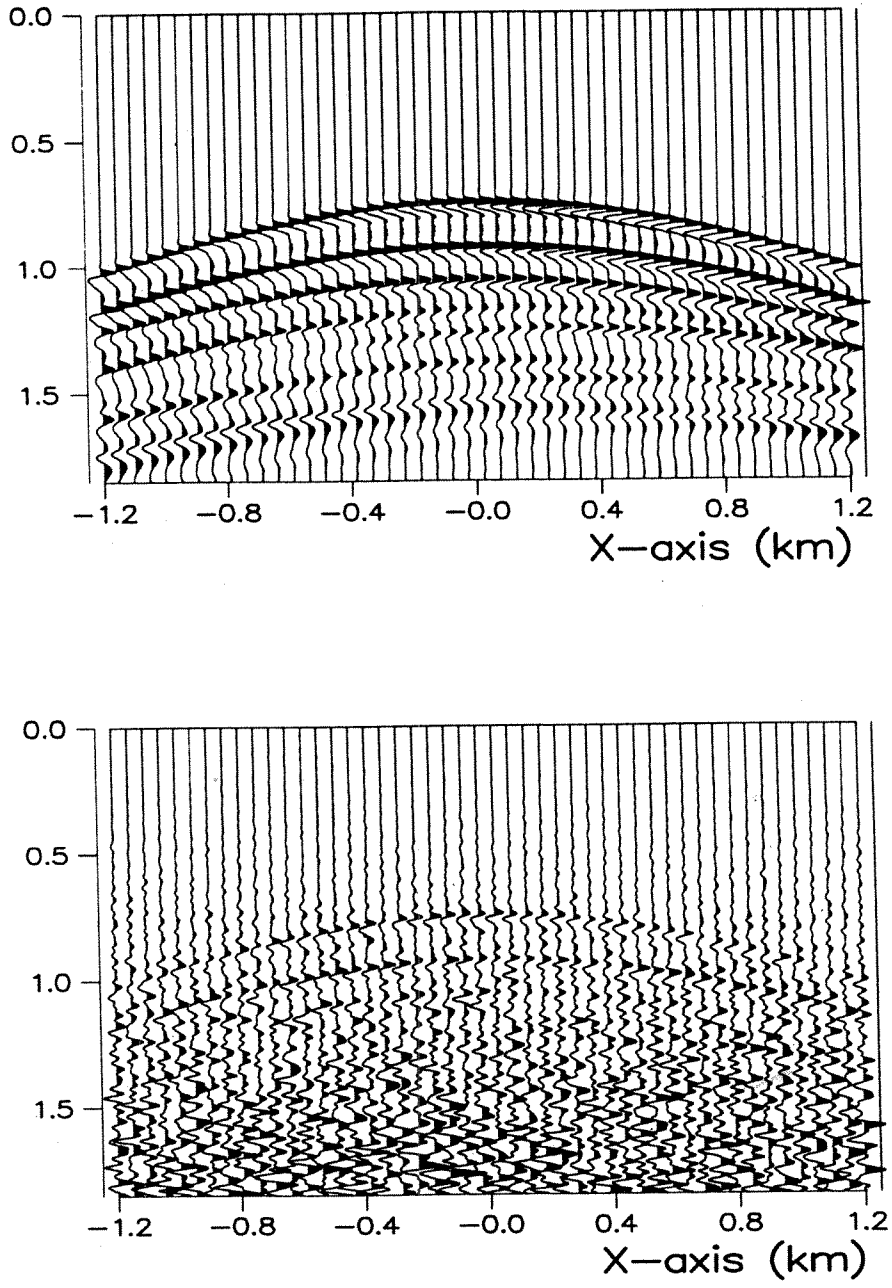

Fig. 3. Common-receiver gather for the second receiver. The direct wave has been partly attenuated by subtracting the data modelled in the macro-model. The data are scaled with t^2. The data in the top and bottom panels are equal, except for the presence of noise in the bottom panel.

Reference migration

To check the ability of the viscoacoustic algorithm to suppress the effects of dissipation, a set of acoustic data was also generated. The acoustic model was obtained by replacing the quality factors in Table 1 by infinite quality factors. The acoustic data were migrated by an acoustic version of our migration scheme, using acoustic extrapolation and the dissipation-free weighting operator (5). This reference image is shown in Fig. 4. In Figs. 4, 5 and 6, we also show images obtained as the sum of (weighted) crosscorrelations of the vertical and horizontal components of the acceleration wavefields. These images are interesting in the case of dissipative media because dissipation is a frequency-dependent process, and the pressure and acceleration wavefields cover different frequency bands. The exact model is plotted as background for the images. Since the autocorrelation has zero phase, the imaged reflectors are centred about their correct location. The deepest reflector corresponds to a decrease in impedance, and therefore has a negative polarity. The polarity of the two types of images is different because the reflection coefficients for pressure and acceleration (or displacement) are opposite. The bottom image is slightly more high-frequent and noisy. Multiple energy creates small horizontal artefacts at about 2.35 km and 2.65 km depth.

Acoustic migration

Migrating the viscoacoustic data in top of Fig. 3 with the acoustic algorithm provides the images in Fig. 5. The effect of attenuation shows up as poor resolution in the top image and as a decrease of reflectivity with depth in the bottom image. Due to the phase errors introduced by velocity dispersion, the images are not centred about the exact location of the reflectors, and the distance between the two deepest reflectors seems to be different on the two images.

The reason why dissipation affects the two images differently is that the accelerations are more high-frequent than the pressure. In Fig. 2, we have plotted the phase velocity and the function $e^{-\alpha(\omega)l}$, where l and $\alpha(\omega)$ (attenuation factor) were chosen to represent average properties of the medium for a wave reflected in the center of the target area. The pressure wavefields undergo severe phase and amplitude distortion, which deform the pulse shape and decrease the resolution. In the acceleration wavefields, the shape of the amplitude and phase spectra is less affected, but the total amount of attenuation is higher.

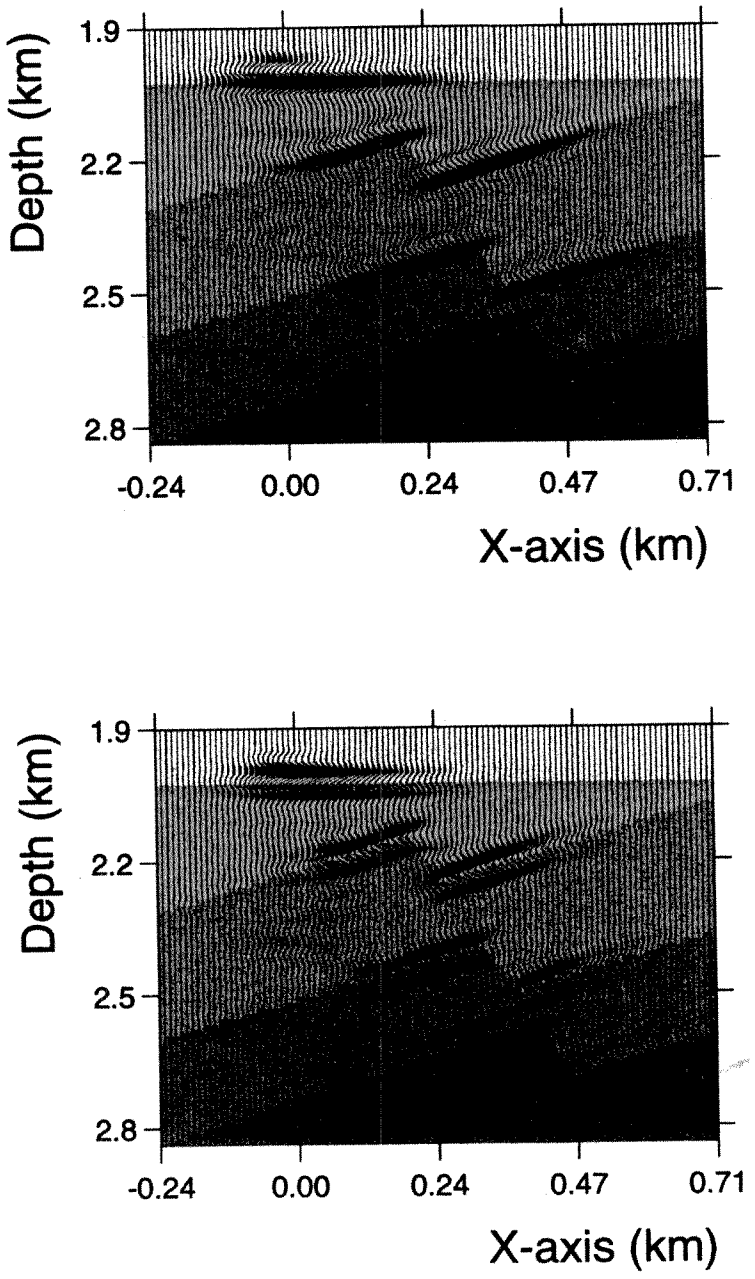

Fig. 4. Acoustic migration of acoustic data (reference). Image from pressure (top) and acceleration wavefields (bottom).

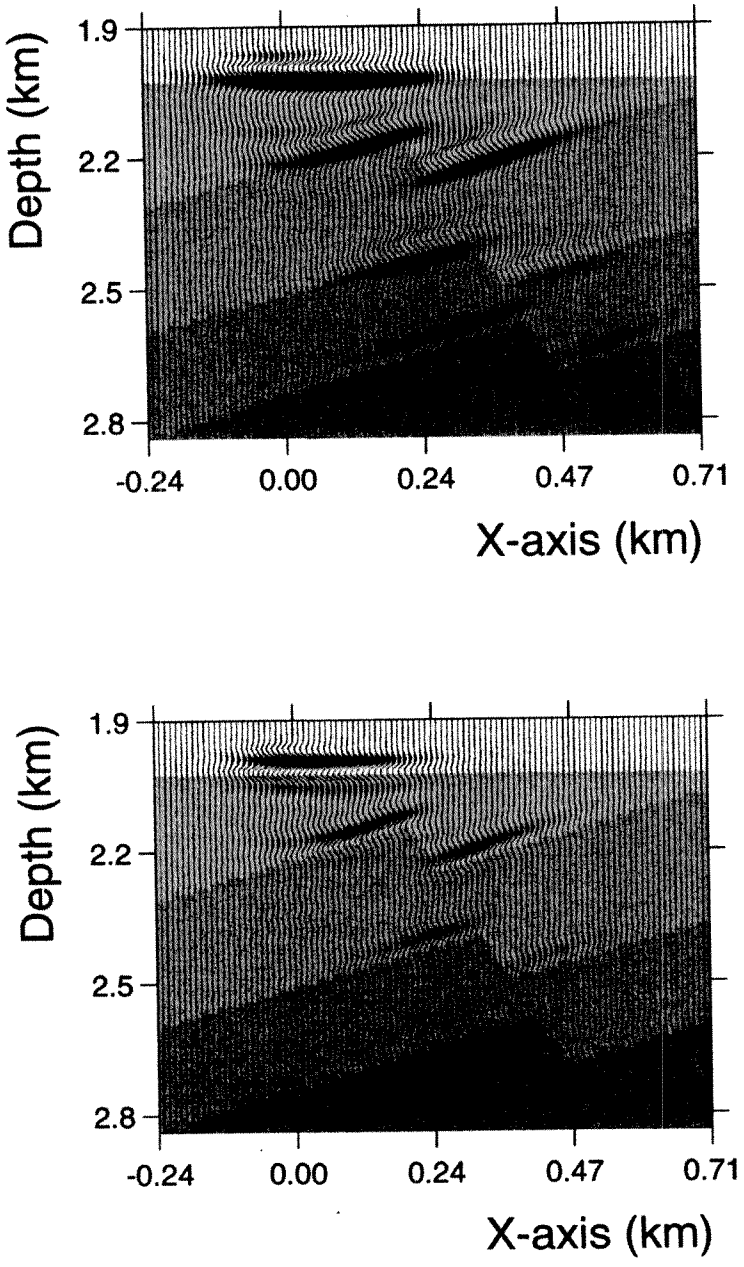

Fig. 5. Acoustic migration of the viscoacoustic data. Image from pressure (top) and acceleration wavefields (bottom).

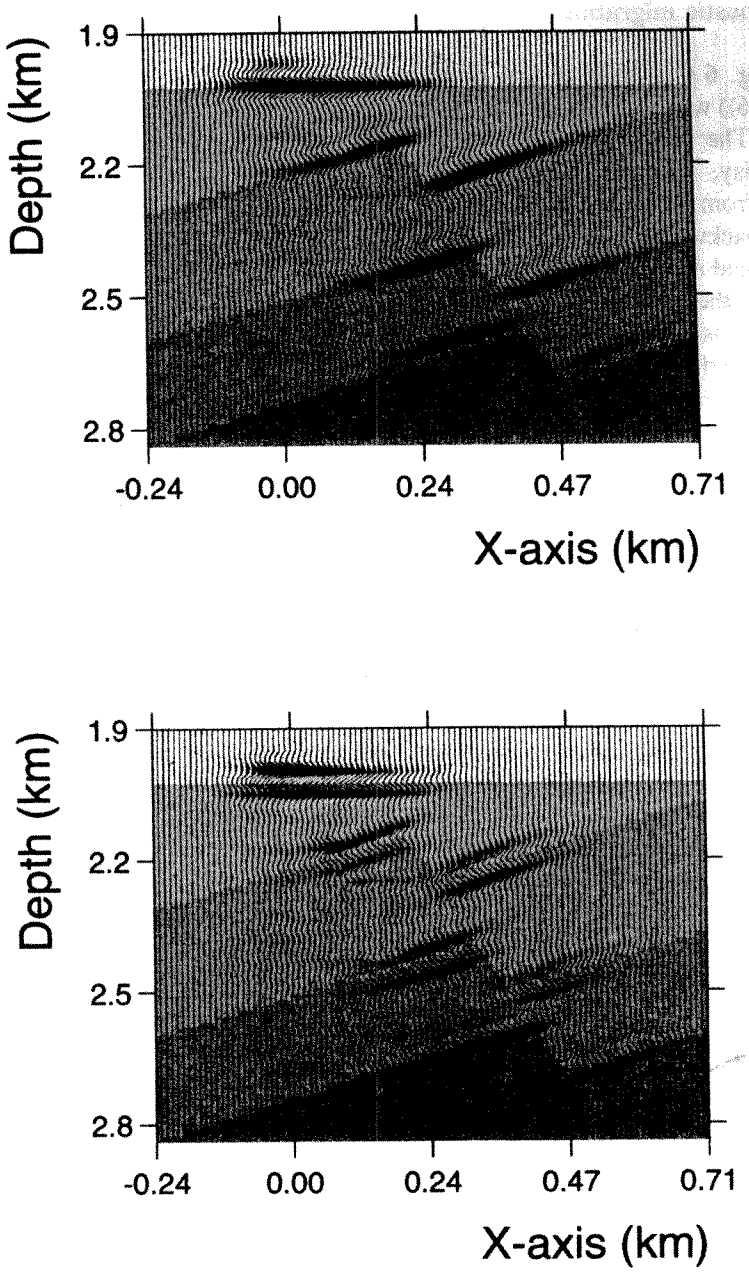

Fig. 6. Viscoacoustic migration of the viscoacoustic data. Image from pressure (top) and acceleration wavefields (bottom).

Viscoacoustic migration

Fig. 6 shows the images obtained by viscoacoustic migration (Equations (2) and (6)) with the correct macro-model (low-pass filtered version of the exact model). The images are quite similar to the reference images, though slightly more noisy, and covering a smaller part of the real reflectors. The artefacts coming from multiple energy are slightly stronger and at a different location. During backward extrapolation in the smooth macro-model, multiple energy is extrapolated as primary energy: because attenuation and dispersion in the model present rather important vertical and lateral variations, the correction for absorption is not exact for the multiples. In the model used in this test, the general trend is an increase of dissipation with depth. Hence, the multiples are overcorrected for dissipation effects during the extrapolation.

Since this method involves the boosting of high-frequent energy during the extrapolation, it is important to test it on noisy data. Noise with random phase and the same frequency band as the source function was added to the three gathers (see bottom of Fig. 3). Although strong compared to the reflected signals from the dipping interfaces, the noise apparently does not deteriorate the results of migration (Fig. 7). Other types of noise were tested, which gave similar results. Several things may explain the robustness of our scheme in the presence of noise:

1. Our implementation of modelling with amplification is numerically stable (Causse et al., 1999).

2. Since we use a standard linear solid rather than a constant-Q model, the amplitude decay reaches a positive minimum value at high frequencies rather than going towards zero. Therefore, the amplification factor does not go towards infinity at large frequencies during the numerical extrapolation with amplification.

3. The cross-correlation with the downgoing field acts as a band-pass filter on the upgoing field, which attenuates possible noise in the high-frequency range.

4. The backward extrapolation (assuming the aperture is large enough) focuses the reflected signals, increasing the signal-to-noise ratio significantly. In the zero-offset migration example presented by Dai and West (1994), the noise at large times is boosted by the compensation for dissipation.

In practice, the estimation of quality factors may be a difficult task. To check the sensitivity of the method with respect to the quality of the dissipation

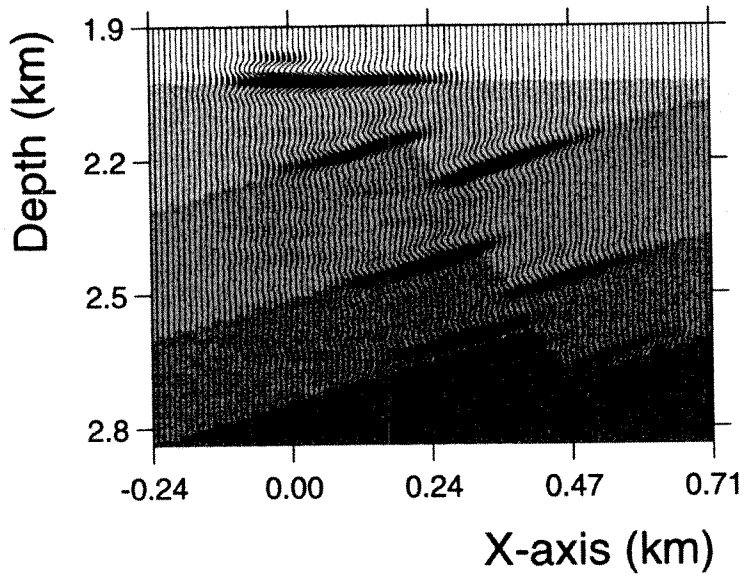

Fig. 7. Viscoacoustic migration of noisy viscoacoustic data (image from pressure wavefields).

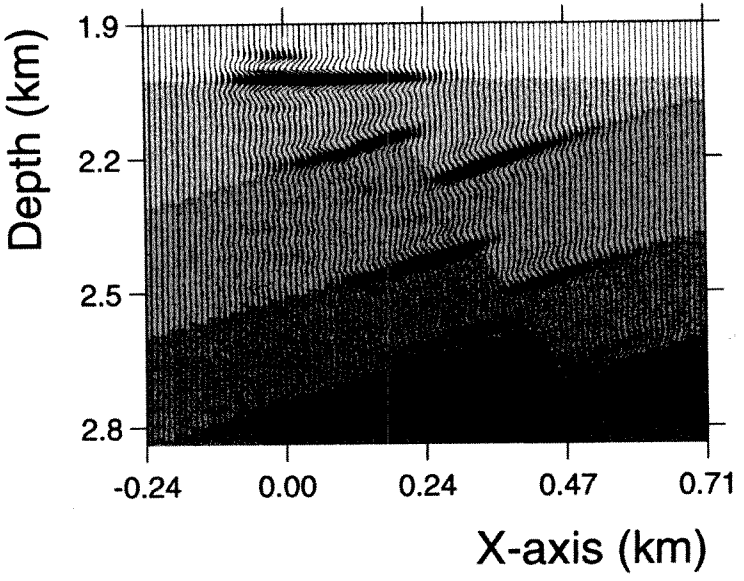

Fig. 8. Viscoacoustic migration with an homogeneous dissipation model (image from pressure wavefields).

model, we performed a migration where the macro-model was obtained by replacing the quality factors and relaxation frequencies in Table 1 by the values $Q_{min} = 35$ and $\omega_0/2\pi = 20$ Hz in the whole model (Fig. 8). Despite this rough dissipation model, the compensation for the dissipation effects improves the quality of the images significantly compared to acoustic migration. This test supports other results suggesting that seismic data and images are not sensitive to the details of the attenuation model (Sollie and Mittet, 1994; Duren and Trantham, 1996; Toverud and Ursin, 1999).

CONCLUSIONS

We have presented a reverse-time migration algorithm that compensates for the effects of absorption (attenuation and dispersion) on migration, by amplifying the downgoing and upgoing wavefields during the forward and backward extrapolations. The method provides a means of obtaining true-amplitude migration in dissipative areas and improving the resolution, provided a macro-model for dissipation is available. A 2-D finite-difference viscoacoustic implementation of the method was tested on synthetic VSP data. The tests illustrated the deterioration of the amplitudes and resolution when absorption is neglected, and demonstrated the low sensitivity of the method to uncorrelated noise and to inaccuracies in the macrodissipation model. A model that roughly reproduces the macroscopic effects of dissipation, irrespective of the physical nature of the attenuation mechanism gives much better images than an unphysical acoustic model that assumes infinite quality factors.

ACKNOWLEDGMENTS

We thank Egil Tjåland for comments on the manuscript. Emmanuel Causse thanks Statoil for financial support.

REFERENCES

Amundsen, L., 1993. Estimation of source array signatures. Geophysics, 58, 1865-1869.
Amundsen, L. and Mittet, R., 1994. Estimation of phase velocities and Q-factors from zero-offset vertical seismic profile data. Geophysics, 59: 500-517.
Berkhout, A.J. and Wapenaar, C.P.A., 1989. One-way versions of the Kirchhoff integral. Geophysics, 54: 460-467.
Bourbié, T, Coussy, O. and Zinszner, B., 1987. Acoustics of Porous Media. Editions Technip, Paris.
Bickel, S.H. and Natarajan, R.R., 1985. Plane-wave Q-deconvolution. Geophysics, 50: 1426-1439.
Causse, E., Mittet, R. and Ursin, B., 1999. Preconditioning of full-waveform inversion in viscoacoustic media. Geophysics, 64: 130-145.
Causse, E. and Ursin, B., 1999. Asymptotic error analysis of constant velocity viscoacoustic migration. Geophysics, 64: 1036-1045.

Claerbout, J.F., 1971. Toward a unified theory of reflector mapping. Geophysics, 36: 467-481.
Dai, N. and West, G.F., 1994. Inverse Q-migration. Expanded Abstr., 64th Ann. Internat. SEG Mtg., Los Angeles: 1418-1421.
De, G.S., Winterstein, D.F. and Meadows, M.A., 1994. Comparison of P- and S-wave velocities and Q's from VSP and sonic log data. Geophysics, 59: 1512-1529.
Duren, R.E. and Trantham, E.C., 1996. Sensitivity of the dispersion correction to Q errors. Geophysics, 61: 288-290.
Emmerich, H. and Korn, M., 1987. Incorporation of attenuation into time-domain computations of seismic wave fields. Geophysics, 52: 1252-1264.
Esmeroy, C. and Oristaglio, M., 1988. Reverse-time wave-field extrapolation, imaging and inversion. Geophysics, 53: 920-931.
Gray, S.H., 1997. True-amplitude seismic migration: A comparison of three approaches. Geophysics, 62: 929-936.
Hargreaves, N.D. and Calvert, A.J., 1991. Inverse Q-filtering by Fourier transform. Geophysics, 56: 519-527.
Harris, P.E., Kerner, C. and White, R.E., 1997. Multichannel estimation of frequency-dependent Q from VSP data. Geophys. Prosp., 45: 87-109.
Holberg, O., 1987. Computational aspects of the choice of operator and sampling interval for numerical differentiation in large-scale simulation of wave phenomena. Geophys. Prosp., 35: 629-655.
Kosloff, D.D. and Baysal, E., 1983. Migration with the full acoustic wave equation. Geophysics, 48: 677-687.
Landrø, M., Langhammer, J., Sollie, R., Amundsen, L. and Berg, E., 1994. Source signature determination from ministreamer data. Geophysics, 59: 1261-1269.
Landrø, M. and Sollie, R., 1992. Source signature determination by inversion. Geophysics, 57: 1633-1640.
Levin, A.S., 1984. Principle of reverse-time migration. Geophysics, 49: 581-583.
McMechan, G.A., 1983. Migration by extrapolation of time-dependent boundary values. Geophys. Prosp., 31: 413-420.
Mittet, R., 1994. Implementation of the Kirchhoff integral for elastic waves in staggered-grid modeling schemes. Geophysics, 59: 1894-1901.
Mittet, R. and Hokstad, K., 1995. Transforming walkaway VSP data into reverse VSP data. Geophysics, 60: 968-977.
Mittet, R., Sollie, R. and Hokstad, K., 1995. Prestack depth migration with compensation for absorption and dispersion. Geophysics, 60: 1485-1494.
Morse, P.M. and Feshbach, H., 1953. Methods of Theoretical Physics. McGraw-Hill Book Co., New York.
Nicolétis, L., Svay-Lucas, J., Clochard, V. and Comte, P., 1997. 3-D true-amplitude migration of 3-C compressional and converted shear waves. J. of Seismic Explor., 6: 127-142.
Robinson, J.C., 1979. A technique for the continuous representation of dispersion in seismic data. Geophysics, 44: 1345-1351.
Schleicher, J., Tygel, M. and Hubral, P., 1993. 3-D true-amplitude finite offset migration. Geophysics, 58: 1112-1126.
Sollie, R. and Mittet, R., 1994. Prestack depth migration: Sensitivity to macro absorption model. Expanded Abstr., 64th Ann. Internat. SEG Mtg., Los Angeles: 1422--1426.
Stewart, R.R., Huddleston, P.D. and Kan, T.K., 1984. Seismic versus sonic velocities: A vertical seismic profile study. Geophysics, 49: 1153--1168.
Toverud, T. and Ursin, B., 1999. Estimation of viscoacoustic parameters from zero-offset VSP data. Expanded Abstr., EAGE Conf., Helsinki: 4-29.
Wapenaar, C.P.A., Peels, G.L., Budejicky, V. and Berkhout, A.J., 1989. Inverse extrapolation of primary seismic waves. Geophysics, 54: 853-863.

APPENDIX A

Representation theorem for forward and backward viscoacoustic extrapolation

The derivations of the representation integrals for nondissipative media are well-known (e.g., Morse and Feshbach, 1953; Wapenaar et al., 1989). For dissipative media, the derivations are more subtle because the wave equation is no longer self-adjoint (i.e., is not symmetrical with respect to time). We describe the viscoacoustic medium at each point $\mathbf{x}$ in the subsurface by the inverse density or lightness $L(\mathbf{x})$ and the bulk compressibility $c(\mathbf{x},t)$ (inverse of the bulk modulus), which we let be time-dependent to account for the dissipation of waves. We will use the Fourier transform with respect to time, and denote the frequency representation of time-dependent quantities with capital letters (e.g., $C(\mathbf{x},\omega)$ for the compressibility). The wave equation for pressure can be written as

$$[\omega^2 C(\mathbf{x},\omega) + \partial_i L(\mathbf{x})\partial_i]P(\mathbf{x},\omega) = -F(\mathbf{x},\omega) \quad , \tag{A-1}$$

with Einstein's summation convention, where $F(\mathbf{x},\omega)$ is the frequency representation of the sources. We are interested in the solution $p(\mathbf{x},t)$ to this scalar wave equation for $\mathbf{x}$ inside a volume V_0 and $t \in [0;T]$, where T is the recording time. We assume that the source function vanishes for $t > T_0$ (with $T \gg T_0$). For this solution to be uniquely defined, we need boundary conditions on the surface S_0 enclosing V_0, as well as time conditions. In practice, S_0 represents the edges of our model or grid, and we can assume homogeneous boundary conditions on the parts of S_0 representing free surfaces, and radiation conditions (simulated by absorbing boundaries) on the rest of the surface. The (initial) time conditions are

$$p(\mathbf{x},t) = 0 \qquad \text{for } t < 0, \quad \mathbf{x} \in V_0. \tag{A-2}$$

This solution can be expressed using the Green's function $g(\mathbf{x},\mathbf{x}_0,t)$, with Fourier transform $G(\mathbf{x},\mathbf{x}_0,\omega)$, defined as a solution to the wave equation,

$$[\omega^2 C(\mathbf{x},\omega) + \partial_i L(\mathbf{x})\partial_i]\, G(\mathbf{x},\mathbf{x}_0,\omega) = -\delta(\mathbf{x} - \mathbf{x}_0) \quad , \tag{A-3}$$

with the same boundary conditions on S_0 as for p, and (initial or final) time conditions that will be specified later.

We multiply equation (A-1) by $G(\mathbf{x},\mathbf{x}_0,\omega)$ and equation (A-3) by $P(\mathbf{x},\omega)$, subtract and integrate over $\mathbf{x}$ in the volume V_0. Using Gauss' theorem, we obtain

$$\begin{aligned} P(\mathbf{x}_0,\omega) = & \int_{V_0} d\mathbf{x}\; G(\mathbf{x},\mathbf{x}_0,\omega)F(\mathbf{x},\omega) \\ & + \int_{S_0} d\mathbf{x}\; n_i(\mathbf{x})L(\mathbf{x})[G(\mathbf{x},\mathbf{x}_0,\omega)\partial_i P(\mathbf{x},\omega) \\ & - P(\mathbf{x},\omega)\partial_i G(\mathbf{x},\mathbf{x}_0,\omega)] \quad , \end{aligned} \tag{A-4}$$

for any point $\mathbf{x}_0$ in V_0, where n_i represents the component of the outward-pointing unit vector orthogonal to S_0 in direction i. For $\mathbf{x}_0$ outside V_0, the left-hand side in this equation vanishes. Going back to the time-domain, we obtain the representation theorem, valid for all points $\mathbf{x}_0$ inside V_0:

$$\begin{aligned} p(\mathbf{x}_0,t_0) = & \int_{V_0} d\mathbf{x} \int_0^{T_0} dt\; g(\mathbf{x},\mathbf{x}_0,t_0-t)f(\mathbf{x},t) \\ & + \int_{S_0} d\mathbf{x}\; n_i(\mathbf{x})L(\mathbf{x}) \int_0^{\infty} dt\; [g(\mathbf{x},\mathbf{x}_0,t_0-t)\partial_i p(\mathbf{x},t) \\ & - p(\mathbf{x},t)\partial_i g(\mathbf{x},\mathbf{x}_0,t_0-t)] \quad . \end{aligned} \tag{A-5}$$

Using the representation theorem for the particular field $g(\mathbf{x},\mathbf{x}',t_0)$, for $\mathbf{x}'$ in V_0, with the homogeneous boundary conditions on S_0, we get

$$g(\mathbf{x}_0,\mathbf{x}',t_0) = g(\mathbf{x}',\mathbf{x}_0,t_0) \quad , \tag{A-6}$$

which is an expression of the reciprocity theorem.

We now introduce time conditions for the Green's function, and denote g^+ the causal solution (verifying $g^+(\mathbf{x},\mathbf{x}_0,t) = 0$, for $t < 0$) and g^- the anti-causal solution (verifying $g^-(\mathbf{x},\mathbf{x}_0,t) = 0$, for $t > 0$). The function $g^+(\mathbf{x},\mathbf{x}_0,t)$ can be thought of as a wavefront expanding from a point source at $\mathbf{x}_0$ as time t increases from 0. The function $g^-(\mathbf{x},\mathbf{x}_0,t)$ represents a wavefront collapsing towards $\mathbf{x}_0$ as time increases towards 0. Both g^+ and g^- are attenuated as t increases. The representation theorem (A-5) is valid for both Green's functions, but may be simplified when selecting one of the two solutions.

Forward wavefield extrapolation

Taking the causal Green's function g^+, considering the homogeneous boundary conditions on surface S_0, and using the reciprocity theorem (A-6) in the representation theorem (A-5), we obtain

$$p(\mathbf{x}_0,t_0) = \int_{V_0} d\mathbf{x} \int_0^{T_0} dt\; g^+(\mathbf{x}_0,\mathbf{x},t_0-t)f(\mathbf{x},t) \quad . \tag{A-7}$$

This equation represents a forward extrapolation (modelling) of the pressure wavefield p.

Backward wavefield extrapolation

For the backward wavefield extrapolation, we use the anti-causal Green's function g^-, and we again consider the representation theorem (A-5). But now, we use an integration volume V included in V_0, bounded by surface S, which represents the recording surface. The volume integral vanishes for $t_0 > T_0$. This integral is necessary to ensure the causality condition (A-2), but usually we are not interested in the wavefield for times smaller than the source duration T_0, and we can therefore neglect it. We assume that T is large enough for the wavefield to totally escape from the volume V within T seconds. Then, we can replace the upper bound of the time integral by T in Equation (A-5). Using the reciprocity theorem, we obtain the Kirchhoff integral for the viscoacoustic wavefield:

$$p(\mathbf{x}_0,t_0) \simeq \int_S d\mathbf{x}\, n_i(\mathbf{x})L(\mathbf{x}) \int_0^T dt[g^-(\mathbf{x}_0,\mathbf{x},t_0-t)\partial_i p(\mathbf{x},t) - p(\mathbf{x},t)\partial_i g^-(\mathbf{x}_0,\mathbf{x},t_0-t)] \quad . \tag{A-8}$$

This represents a reconstruction of the pressure wavefield (backward extrapolation) from the records of the pressure and its normal derivative on S. Equation (A-8) holds for $\mathbf{x}_0 \in V$. When $\mathbf{x}_0$ is outside V, the left-hand side vanishes. Hence, the reconstructed wavefield is exactly equal to p inside the recording surface, but is zero outside (for a numerical illustration, see Mittet, 1994). In practice, the pressure wavefield can be reconstructed using one type of boundary conditions only, because the contributions from the two types of boundary conditions are equal inside V (Berkhout and Wapenaar, 1989). Of course, in reality the recording surface is not closed, and the wavefield reconstruction is only approximate.

For the practical implementation of the backward wavefield extrapolation, it is convenient to introduce a fictive amplifying medium with lightness L_A and compressibility c_A defined as

$$L_A(\mathbf{x}) = L(\mathbf{x}) \quad , \tag{A-9}$$

$$c_A(\mathbf{x},t) = c(\mathbf{x},-t) \quad , \tag{A-10}$$

or, in the frequency-domain, $C_A(\mathbf{x},\omega) = C^*(\mathbf{x},\omega)$. The Green's function in the amplifying medium is denoted $g_A(\mathbf{x},\mathbf{x}_0,t)$, with causal and anti-causal solutions g_A^+ and g_A^-. Obviously, $G_A^*(\mathbf{x},\mathbf{x}_0,\omega)$ satisfies the same equation as $G(\mathbf{x},\mathbf{x}_0,\omega)$. Hence, considering the causal and anti-causal conditions, we have

$$g^-(\mathbf{x},\mathbf{x}_0,t) = g_A^+(\mathbf{x},\mathbf{x}_0,-t) \quad . \tag{A-11}$$

Introducing this equation into Equation (A-8) with suitable variable changes in the integrals, we obtain

$$p(\mathbf{x}_0,T-t_0) \simeq \int_V d\mathbf{x} \int_0^T dt\, g_A^+(\mathbf{x}_0,\mathbf{x},t_0-t) [\int_S d\mathbf{x}'\, n_i(\mathbf{x}')L(\mathbf{x}')\partial_i' p(\mathbf{x}',T-t)\delta(\mathbf{x}-\mathbf{x}') + \int_S d\mathbf{x}'\, n_i(\mathbf{x}')L(\mathbf{x}')p(\mathbf{x}',T-t)\partial_i\delta(\mathbf{x}-\mathbf{x}')] \quad . \tag{A-12}$$

Comparing with the modelling Equation (A-7), we see that the same scheme that is used for forward modelling in the viscoacoustic medium may also be used for the backward extrapolation of the wavefield p, by 1) reversing the order of the time samples in the records, 2) replacing the original medium parameters by the parameters of the fictive amplifying (adjoint) medium, 3) applying the viscoacoustic modelling scheme with the records as sources, 4) reversing the order of the time samples in the obtained extrapolated wavefield. Note that backward wavefield extrapolation in lossless media is usually performed in the same way (McMechan, 1983; Esmeroy and Oristaglio, 1988), but without the need for step 2), because the acoustic and elastic wave equations are self-adjoint (symmetrical in time). With the procedure for attenuating media, high frequencies attenuated during the propagation in the viscoacoustic medium are boosted during the backward propagation.

Causse et al. (1999) explain in detail in their Appendix D how to do the required extrapolation with amplification in a stable way by finite-difference modelling, for viscoacoustic earth models described as standard linear solids (see Appendix B). A standard linear solid and its adjoint have exactly the same parameters, except for the sign of the relaxation frequency ω_0. The negative relaxation frequencies required for extrapolation in the adjoint of the attenuating medium generate growing exponentials that cause instability. If ω_0 remains positive, however, numerically stable extrapolation with amplification can be performed by choosing ΔM negative (note that if both ω_0 and ΔM are negative, the extrapolation is numerically instable although attenuating). If ΔM is chosen properly, one can obtain a wavefield with the correct amplitude spectrum (i.e., the correct frequency-dependent amplification), but with an incorrect phase spectrum (i.e., an incorrect velocity dispersion). However, the correct phase spectrum can be extracted from the attenuated wavefield. The appropriate wavefield can therefore be obtained by combining the results of two finite-difference modellings.

APPENDIX B

Standard linear solid

The standard linear solid is a rheological model involving one single relaxation mechanism, with bulk modulus

$$M(\omega) = 1/C(\omega) = M_U + [\Delta M/\{(i\omega/\omega_0) - 1\}] \ , \qquad \text{(B-1)}$$

where M_U is the unrelaxed bulk modulus, ΔM is the difference between the unrelaxed and relaxed bulk moduli, and ω_0 is the relaxation angular frequency (Emmerich and Korn, 1987).

The average between the phase velocities at zero and infinite frequency is

$$V_P = [\sqrt{M_U} + \sqrt{(M_U - \delta M)}]/2\sqrt{\rho} \ , \qquad \text{(B-2)}$$

with $\rho = 1/L$. Defining the quality factor $Q(\omega)$ as the ratio of the real and imaginary parts of the bulk modulus $M(\omega)$ (Bourbié et al., 1987), one can show that $Q(\omega)$ reaches a minimum Q_{min} at angular frequency $\omega = (1 - \Delta M/M_U)^{1/2}\omega_0$, and that

$$Q_{min} = 2(M_U - \delta M)/\Delta M(1 - \delta M/M_U)^{1/2} \ . \qquad \text{(B-3)}$$

The standard linear solid can be parametrized by V_P, Q_{min} and ω_0 rather than M_U, ΔM and ω_0. Equations (B-2) and (B-3) can be inverted, yielding

$$M_U = \rho V_P^2[1 - Q_{min} + \sqrt{(Q_{min}^2 + 1)}]^2 \qquad \text{(B-4)}$$

and

$$\Delta M = 4\rho V_P^2[\sqrt{(Q_{min}^2 + 1)} - Q_{min}] \ . \qquad \text{(B-5)}$$